Supporting Information File:

Mechanistic insight into biopolymer induced iron oxide mineralization through quantification of molecular bonding

K.K. Sand*[a,b]1,2, S. Jelavić[c]2, S. Dobberschütz[c], P. D. Ashby[b], M.J. Marshall[d], K. Dideriksen[c]3, S.L.S. Stipp[c]4, S.N. Kerisit[a], R.W. Friddle[e] and J.J. DeYoreo*[a,f]

[a] Physical Sciences Division, Pacific Northwest National Laboratory, Richland, WA, USA

[b] Molecular Foundry, Lawrence Berkeley National Laboratory, Berkeley, CA. USA

[c] Nano-Science Center, Department of Chemistry, University of Copenhagen, Denmark

[d] Biologic Sciences Division, Pacific Northwest National Laboratory, Richland, WA, USA

[e] Sandia National Laboratories, Livermore, California 94550, USA

[f] Department of Material Science and Engineering, University of Washington, Seattle, WA, USA

* To whom correspondence may be addressed: kas84@aber.ac.uk, james.DeYoreo@pnnl.gov

Current address:

[1] Geography & Earth Sciences, Aberystwyth University, UK

[2] Section for GeoGenetics, Globe Institute, Faculty of Health and Medical Sciences, University of Copenhagen, Denmark

[3] Department of Geochemistry, Geological Survey of Denmark and Greenland, Denmark

[4] Department of Physics, Technical University of Denmark, Denmark

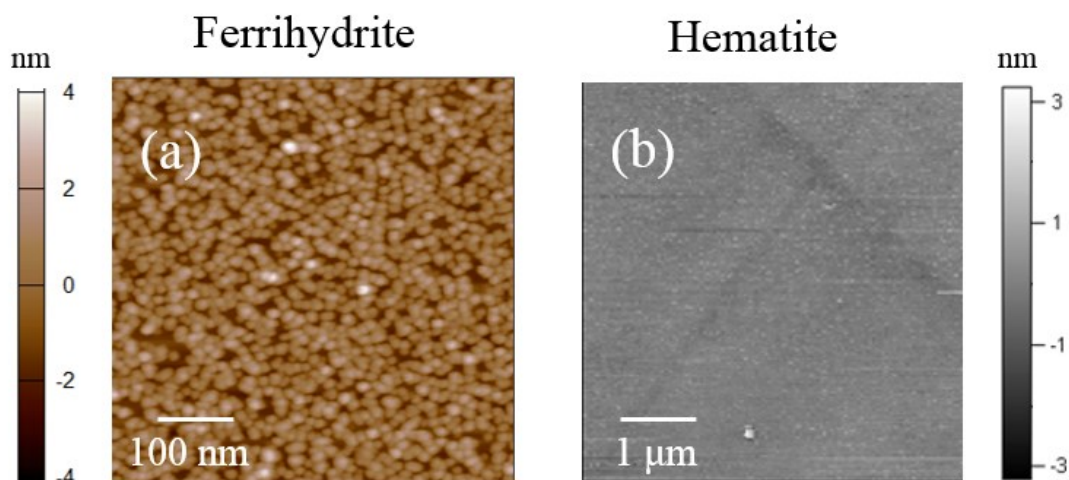## 1. Atomic force microscopy images of ferrihydrite and hematite

Figure S1. AFM images of a) ferrihydrite and b) hematite substrates.
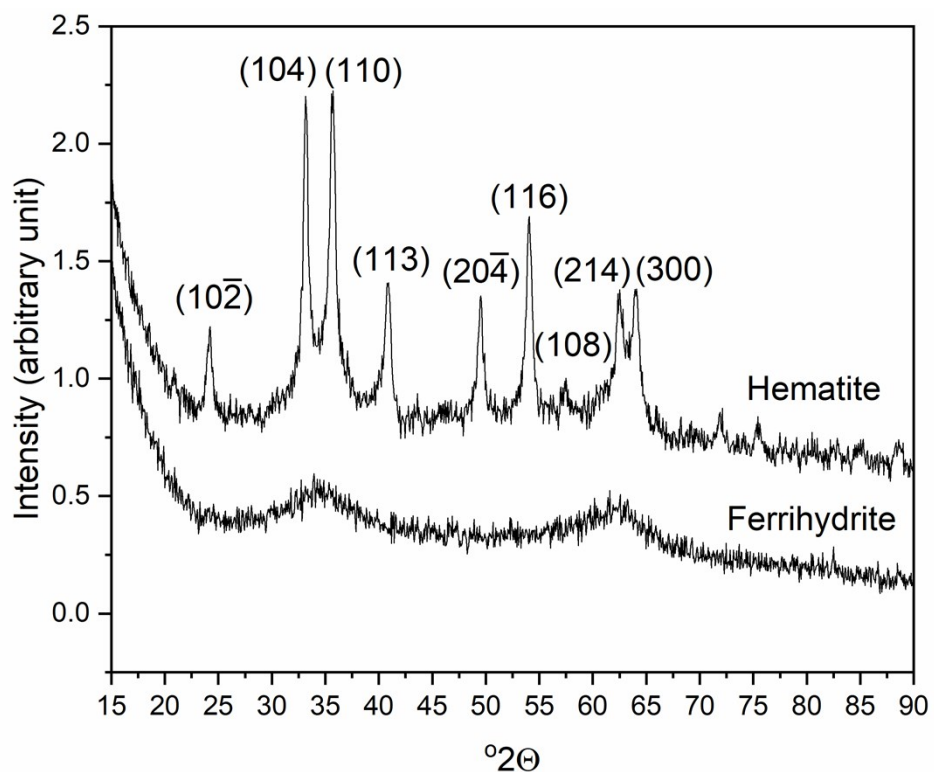

2. X-ray diffraction

Figure S2. XRD traces of hematite and ferrihydrite powders. For hematite, the strongest peaks are indexed and for ferrihydrite, two indicative diffraction bands are present at ~34 ^{0}2Θ and ~63 ^{0}2Θ.
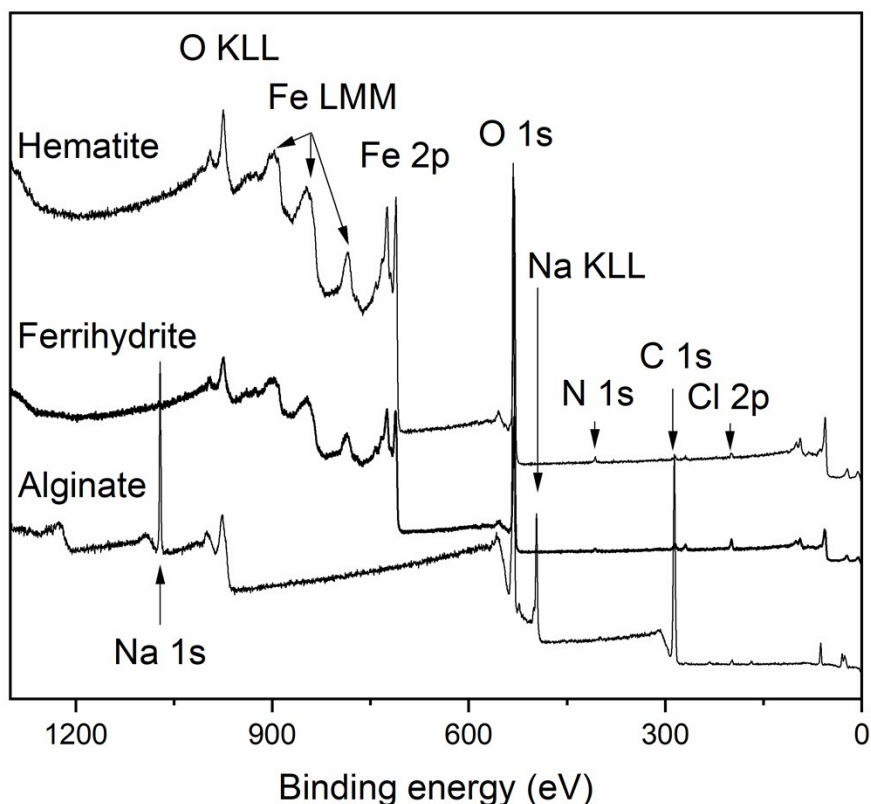
3. X-ray photoelectron spectroscopy

Figure S3. XPS spectra of hematite, ferrihydrite and alginate powders. The photoelectron and Auger transitions are noted above the peaks.

4. Iron (oxyhydr)oxide surface speciation

At pH>pKa for alginate (~ 3.5), the COO^- ligand binds to hydrated iron and provide a binding site for nucleation. Hematite surfaces are positively charged at pH<8 and ferrihydrite, at pH<7.[1] Ferrihydrite $(Fe_{8.2}O_{8.5}(OH)_{7.4}*3H_2O)$[2] is the least stable iron (oxyhydr)oxide phase and is the first phase to form. Ferrihydrite transforms to a range of iron (oxyhydr)oxides, one of which is hematite (α-Fe_2O_3). Hematite is much more stable in air and water under standard conditions than ferrihydrite and has fewer active adsorption sites. Most of the hydroxyl groups on the {00.1} hematite face are doubly coordinated to Fe and have little excess charge to offer in binding.[3,4]
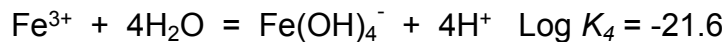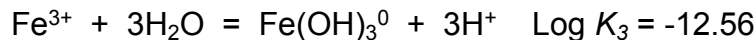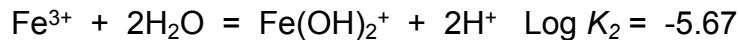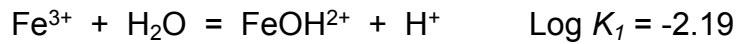
5. Inherent properties of the EPS- and alginate – iron (oxydyr)oxide bond

The complete force spectrum spans a near equilibrium regime (yielding f_{eq} and thus ΔG_{adh}) and a kinetic regime, yielding x_t and k_{off}. The relatively large error found for x_t and k_{off} from fitting the complete model of Friddle et al. (2012)[5] is likely a result of the majority of our force versus loading rate data falling closer to the near equilibrium regime of the spectrum.

6. Iron (oxyhydr)oxide solubility

Equations and data used for geochemical modelling have been taken from PHREEQC, MINTEQ and MINTEQ.v4 databases. To account for differences in equilibrium constants (K) between the databases, we modelled iron speciation, taking all possible values of $\log K$ reported:

PHREEQC:

$Fe^{3+} + H_2O = FeOH^{2+} + H^+$ Log K_1 = -2.19

$Fe^{3+} + 2H_2O = Fe(OH)_2^+ + 2H^+$ Log K_2 = -5.67

$Fe^{3+} + 3H_2O = Fe(OH)_3^0 + 3H^+$ Log K_3 = -12.56

$Fe^{3+} + 4H_2O = Fe(OH)_4^- + 4H^+$ Log K_4 = -21.6

MINTEQ:

$Fe^{3+} + H_2O = FeOH^{2+} + H^+$ Log K_1 = -2.19

$Fe^{3+} + 2H_2O = Fe(OH)_2^+ + 2H^+$ Log K_2 = -5.67

$Fe^{3+} + 3H_2O = Fe(OH)_3^0 + 3H^+$ Log K_5 = -13.6

$Fe^{3+} + 4H_2O = Fe(OH)_4^- + 4H^+$ Log K_4 = -21.6

MINTEQ.v4:

$Fe^{3+} + H_2O = FeOH^{2+} + H^+$ Log K_1 = -2.19

$Fe^{3+} + 2H_2O = Fe(OH)_2^+ + 2H^+$ Log K_6 = -4.594

$Fe^{3+} + 3H_2O = Fe(OH)_3^0 + 3H^+$ Log K_3 = -12.56

$Fe^{3+} + 4H_2O = Fe(OH)_4^- + 4H^+$ Log K_4 = -21.6
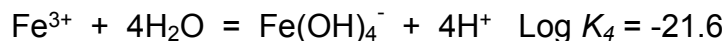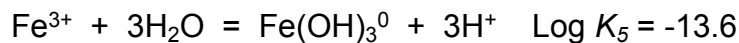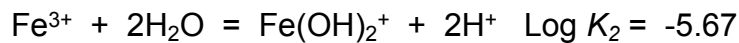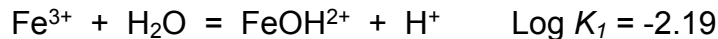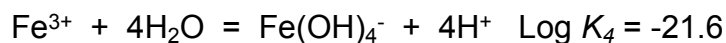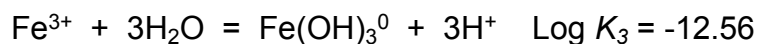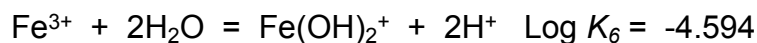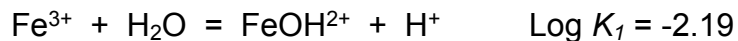
The dominant aqueous iron species, that controls iron (oxyhydr)oxide solubility at pH=5.5, is $Fe(OH)_2^+$ in all three databases. Both reported constants of $logK$ that describe the formation of $Fe(OH)_2^+$ ($logK_2$ and $logK_6$) are taken into account during calculation of solubilities. At pH 7, geochemical speciation determined using the PHREEQC database used $Fe(OH)_3^0$ as a dominant aqueous species but in MINTEQ and MINTEQ.v4 databases, $Fe(OH)_2^+$ is the dominant species, as it was for the system at pH 5.5. Hence, at pH 7, three $logK$ values have been included in the calculation of the solubility of ferrihydrite and hematite: $logK_2$ and $logK_6$ for expressing the equilibrium when $Fe(OH)_2^+$ is the dominant aqueous species and $logK_3$, for when $Fe(OH)_3^0$ dominates.

Solubility for nanoparticles is strongly affected by particle size. This dependence is observed as a solubility product (K_{sp}) that changes with particle size. K_{sp} for 2-line ferrihydrite ranges between 3.4 and 4.0 and for 6-line ferrihydrite, between 3.0 and 3.4.[6] Considering that K_{sp} is inversely proportional to particle size (in the nanometer range) and assuming the relationship to be linear, we tentatively ascribed K_{sp}=4.0 for 2 nm ferrihydrite particles and K_{sp}=3 for 7 nm ferrihydrite.[2] K_{sp} for nanohematite was derived using the approximation of Trolard and Tardy (1987):[7]

$$K_{sp} = -3.886 + \frac{0.025}{d}$$

(S1)

where d represents particle size (µm). The values for K_{sp} for a range of particle sizes for ferrihydrite and hematite, with corresponding solubility data are presented in Table S1.

Table S1. Particle sizes, solubility products (K_{sp}), solubilities (c_{eq}) and interfacial free energies (γ_{CL}) for ferrihydrite and hematite for the 3 databases.

MINTEQ.V4

	FHY			HEM		
		pH 5.5			pH 5.5	
Size (nm)	Ksp	log(Ceq)	γ_{CL} (mJ/m^2)	Ksp	log(Ceq)	γ_{CL} (mJ/m^2)
2	4.00	-6.09	146	8.61	-1.48	62
3	3.80	-6.29	150	4.45	-5.65	138
4	3.60	-6.49	153	2.36	-7.73	176
5	3.40	-6.69	157	1.11	-8.87	197
6	3.20	-6.89	161	0.28	-9.81	214
7	3.00	-7.09	164	-0.31	-10.41	225
8	2.80	-7.29	168	-0.76	-10.86	233
9	2.60	-7.49	172	-1.11	-11.20	240
10	2.40	-7.69	175	-1.39	-11.48	245
15				-2.22	-12.31	260
20				-2.64	-12.73	267
30				-3.05	-13.15	275

MINTEQ

	FHY			HEM		
		pH 5.5			pH 5.5	
Size (nm)	Ksp	log(Ceq)	γ_{CL} (mJ/m^2)	Ksp	log(Ceq)	γ_{CL} (mJ/m^2)
2	4.00	-7.17	166	8.61	-2.56	81
3	3.80	-7.37	169	4.45	-6.72	158
4	3.60	-7.57	173	2.36	-8.81	196
5	3.40	-7.77	177	1.11	-10.06	219
6	3.20	-7.97	180	0.28	-10.89	234
7	3.00	-8.17	184	-0.31	-11.49	245
8	2.80	-8.37	188	-0.76	-11.93	253
9	2.60	-8.57	191	-1.11	-12.28	259
10	2.40	-8.77	195	-1.39	-12.56	264
15				-2.22	-13.39	280
20				-2.64	-13.81	287
30				-3.05	-14.23	295

PHREEQC

	FHY			HEM		
		pH 5.5			pH 5.5	
Size (nm)	Ksp	log(Ceq)	γ_{CL} (mJ/m^2)	Ksp	log(Ceq)	γ_{CL} (mJ/m^2)
2	4.00	-7.17	166	8.61	-2.56	81
3	3.80	-7.37	169	4.45	-6.72	158
4	3.60	-7.57	173	2.36	-8.81	196
5	3.40	-7.77	177	1.11	-10.06	219
6	3.20	-7.97	180	0.28	-10.89	234
7	3.00	-8.17	184	-0.31	-11.49	245
8	2.80	-8.37	188	-0.76	-11.93	253
9	2.60	-8.57	191	-1.11	-12.28	259
10	2.40	-8.77	195	-1.39	-12.56	264
15				-2.22	-13.39	280
20				-2.64	-13.81	287
30				-3.05	-14.23	295

7. Interfacial free energy calculations

We derived γ_{CL} for ferrihydrite and hematite at pH 5.5 for particles from 2 to 10 nm diameter (Table S1). For each pH and particle size, we calculated three different values of γ_{CL} arising from three different databases and took the midrange as an estimate in order to show general trends in change in interfacial energy. The relationships between K_{sp}, particle size and γ_{CL} are shown in Fig. S4.
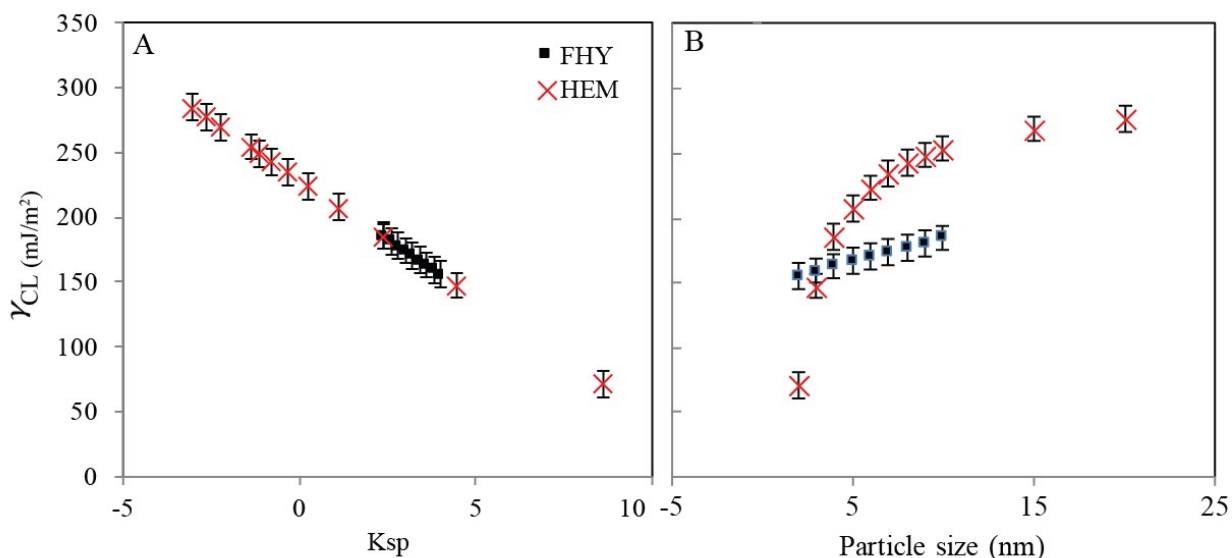
Figure S4. A) Interfacial free energy for the solid-liquid interface (γ_{CL}) as a function of solubility product (K_{sp}). The relationship is linear as a consequence of Söhnel's linear approximation between logarithm of the solubility and the γ_{CL}.[8] B) γ_{CL} as a function of the particle size. For ferrihydrite particles, the relationship is essentially linear. For hematite, the relationship follows the Trolard and Tardy approximation.[7] The error bars correspond to ±10 mJ/m², which is the mean standard error for the midrange values obtained from the 3 databases.

Applying Equation S2 and using c_{eq} for 2 different grain sizes of ferrihydrite and hematite gives the γ_{CL} used in the current study (Table S2). At the pH of this study (5.5), grain size does not have a significant effect on the outcome of the energy barrier ((γ_{CL}) from Table S2 vs. data in Table S1).

Table S2. γ_{CL}, in mJ/m².

γ_{CL}	3 nm	6 nm
Ferrihydrite	159	170

8. Plausible ranges for *a* and *h*

We expect *a* and *h* to vary in a natural system. We present the values for the interfacial free energy, *γ*, obtained for relevant combinations of *a* and *h* (Table 2), to account for a likely range of values. The area of interaction assumed for a saccharide ring length is 0.483 nm.[9] We assume that the area of interaction is localized over the carboxyl, giving l_{mono} = 0.675 nm based on the length of the carboxyl group (0.192 nm). The estimated matrix of plausible ranges of interaction areas are given in Table S3; a range from 0.1 to 0.5 nm^2.

Table S3. Plausible areas of interaction (nm^2) based on unit length (nm) for l_{mono}

Length in nm		0.192	0.48	0.675
Saccharide unit + R-C-O	0.675	0.13	0.32	0.46
Saccharide unit	0.483	0.09	0.23	0.33
R-C-O	0.192	0.04	0.09	0.13

9. Pair distribution function (PDF)

For all samples, there were peaks in the Q[S(Q)-1] and the PDFs at the positions expected for ~2 nm ferrihydrite (Figures S5 and S6).[10,11] However, the presence of alginate during ferrihydrite synthesis resulted in subtle differences, consistent with difference in the size of the coherent scattering domains (CSDs). For the material formed in the presence of alginate, the Q[S(Q)-1] shows slightly decreased intensity for several peaks in the Q range 5-12 Å^{-1} (marked with * in Figure S5), where the ferrihydrite pattern is particularly sensitive to changes in the size of CSDs.[11] Moreover, the third peak of the PDFs, which mostly represents atomic pairs of edge sharing Fe-Fe, is markedly lower in intensity and peak intensity decays more extensively as the interatomic distance increases (Figure S5). All of these features are consistent with changes observed when the ferrihydrite CSDs become smaller.[2] To quantify the changes in CSD size, the measured patterns were fitted with the software PDFgui, which can refine a size based form factor for spherical CSDs. Fits with a single ferrihydrite component, with spherical coherent scattering domains, resulted in calculated patterns that underfit the peaks at higher *r* values (Figure S7; Table S4). Refits with two ferrihydrite components, that were only allowed to differ in scale and CSD size, resulted in better fit to higher *r* peaks but significant discrepancies remained. These misfits could reflect surface relaxation or coherent scattering domains with anisotropic morphology or a distribution of sizes. Nevertheless, we could conclude that the fitting consistently yielded slightly smaller CSDs for the alginate-ferrihydrite complex (~5% smaller diameter; Table S4).
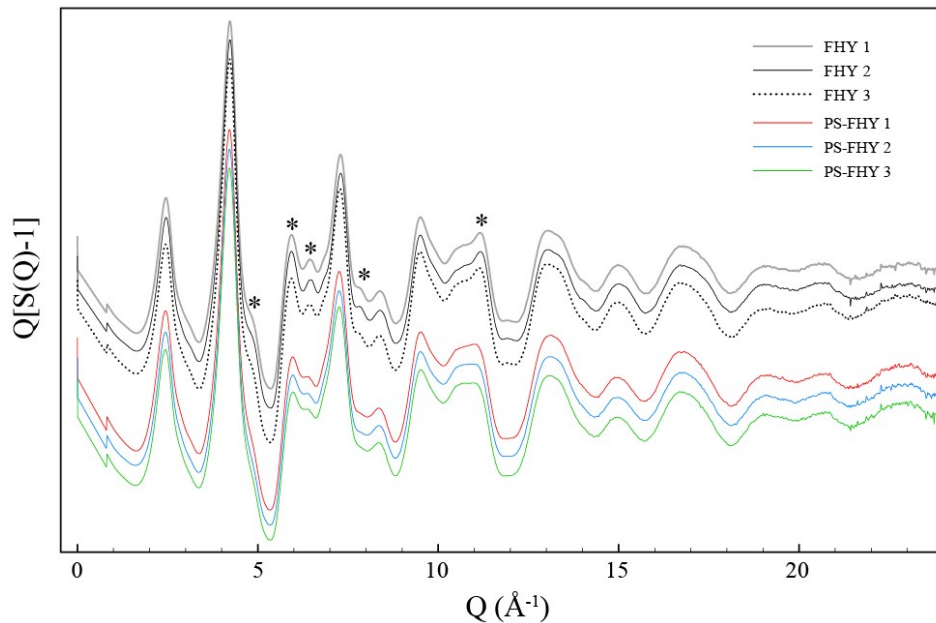
Figure S5. The reduced scattering structure function Q[S(Q)-1] for ferrihydrite (FHY) formed with and without alginate (PS). The functions have been offset for clarity and stars mark peaks where intensity differs for the two types of materials.
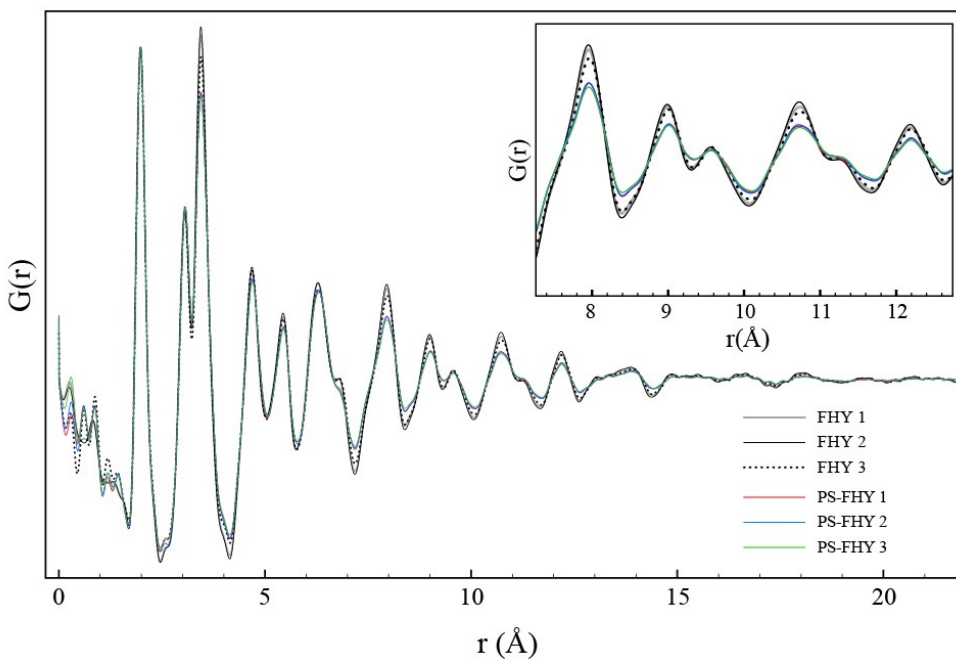
Figure S6. PDFs for ferrihydrite (FHY) formed with and without alginate (PS). The patterns have been normalized to have the same intensity for the Fe-O peak at ~2 Å.

Figure S7. PDFgui fits to the data obtained for ferrihydrite (FHY) formed with and without alginate (PS). Green lines represent fits obtained with a single ferrihydrite component, and red lines, fits with two ferrihydrite components. Inserts show the higher r oscillations at increased resolution.

Table S4. Results of fitting with PDFgui.

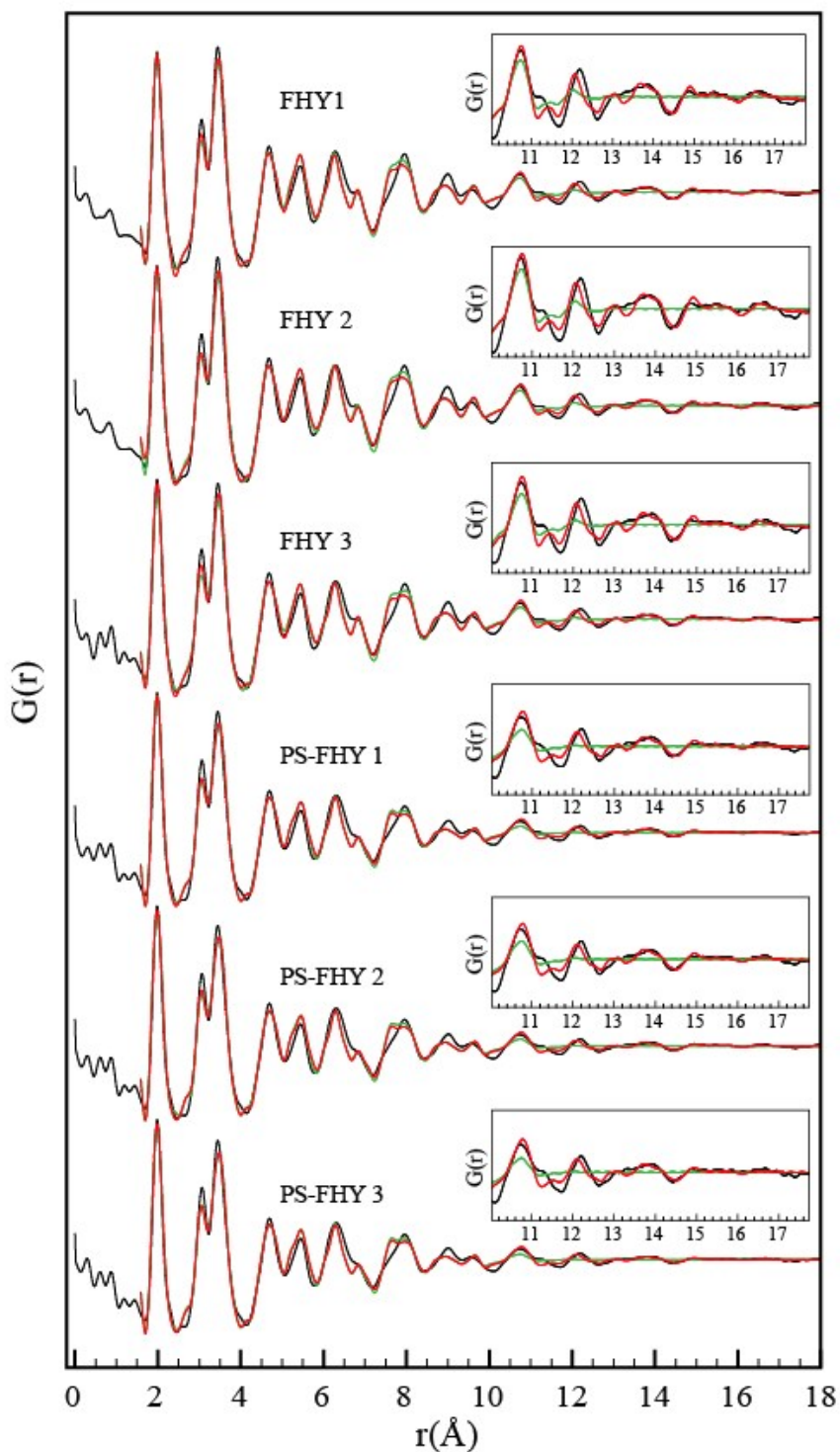| Sample	Component 1 Scale	Size (Å)	Component 2 Scale	Size (Å)	Average Size (Å)	δ_2	Unit cell (Å) a	c	Occupancy Fe1	Fe2	Fe3	U_{iso} (Å²) Fe	O	RW
One component fitting														
Fhyd 1	1	13.6				3.32	5.94	9.05	0.86	0.69	0.92	0.014	0.005	0.21
Fhyd 2	1	13.7				3.02	5.95	9.06	0.82	0.56	1.01	0.014	0.005	0.22
Fhyd 3	1	13.3				3.02	5.96	9.06	0.81	0.42	1.05	0.013	0.006	0.22
Average		13.5±0.4												
Alg Fhyd 1	1	12.6				3.16	5.97	9.03	0.80	0.52	1.01	0.017	0.005	0.21
Alg Fhyd 2	1	12.7				3.14	5.97	9.03	0.76	0.53	0.98	0.017	0.005	0.21
Alg Fhyd 3	1	12.4				3.13	5.97	9.04	0.82	0.55	1.00	0.018	0.004	0.21
Average		12.6±0.3												
Two component fitting														
Fhyd 1	0.75	10.2	0.25	20.8	12.8	3.32	5.95	9.04	0.98	0.73	0.94	0.013	0.004	0.20
Fhyd 2	0.74	9.83	0.26	21.0	12.7	2.91	5.95	9.06	0.94	0.59	0.97	0.014	0.004	0.20
Fhyd 3	0.74	9.91	0.26	20.2	12.6	3.30	5.96	9.05	0.98	0.73	0.91	0.013	0.003	0.20
			Average		12.7±0.3									
Alg Fhyd 1	0.77	9.82	0.23	19.3	12.0	3.17	5.98	9.04	0.91	0.50	1.04	0.017	0.003	0.20
Alg Fhyd 2	0.76	9.86	0.24	19.4	12.1	3.11	5.98	9.04	0.90	0.51	1.01	0.018	0.003	0.19
Alg Fhyd 3	0.76	9.78	0.24	18.62	11.9	3.13	5.98	9.03	0.87	0.47	1.02	0.017	0.004	0.20
			Average		12.0±0.2									

Retrieved values for the relative scale, CSD diameter (Å), averaged dimensions, correlated atomic movement (δ_2), unit cell dimensions, occupancy, isotropic atomic displacement parameters (U_{iso}) and goodness of fit (RW). Fhyd- ferrihydrite, Alg- alginate.

10. Cryogenic X-ray photoelectron spectroscopy (cryoXPS)

Figures S8 and S9 show high resolution spectra of ferrihydrite and hematite O 1s regions. The spectra were acquired for suspensions made with only MiliQ water (Fig. S8a and S9a) and for suspensions made with 0.1% alginate solution (Fig. S8b and S9b). The analyses acquired under cryogenic conditions were called "vitrified" and those acquired at ambient temperature at the same sample but after it was dried in the XPS analysis chamber under high-vacuum (order of magnitude ~10^{-8} Torr) were called "room temperature.

The peak at 530 ± 0.1 eV was attributed to photoemissions from structural oxygens from ferrihydrite and hematite, the peak at at 531.3 ± 0.1 eV to interface hydroxyl groups and 533.1 ± 0.2 eV to water.[12] The contribution from both hydroxyl and water peaks is considered as interfacial water. The interfacial water content was calculated by subtracting the total area of O 1s photoemission of the sample acquired at room temperature from the total area of O 1s photoemission of the sample acquired at cryogenic condition. By doing this, we avoided the contribution from the oxygen in the alginate structure that would otherwise undoubtedly result in higher O content in alginate containing suspensions.
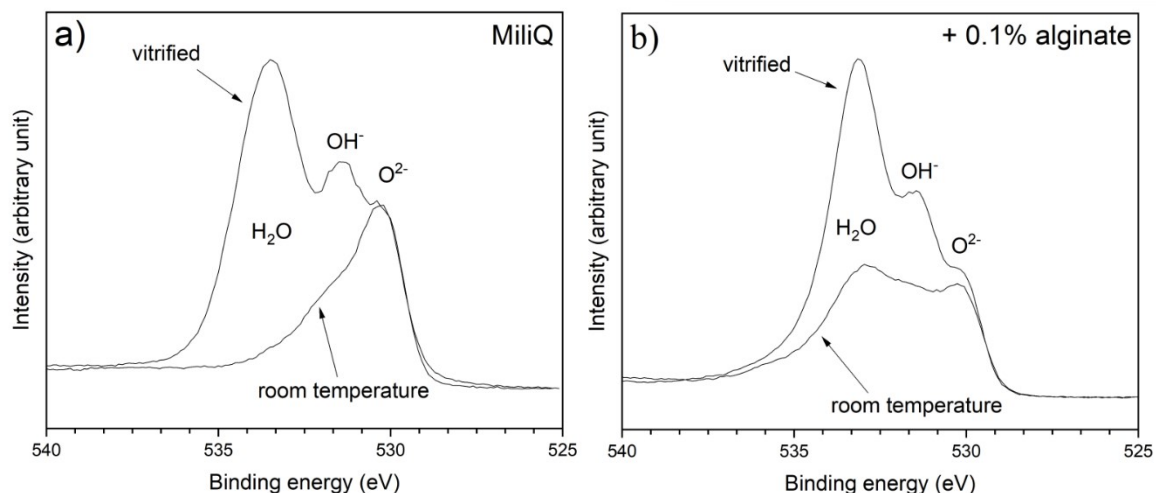

Figure S8. High-resolution XPS spectra of O 1s region for a) pure ferrihydrite and b) alginate-ferrihydrite complex. O^{2-} structural oxygen from ferrihydrite, OH^- - hydroxyl in the ferrihydrite-solution interface region and H_2O- bulk and interfacial water
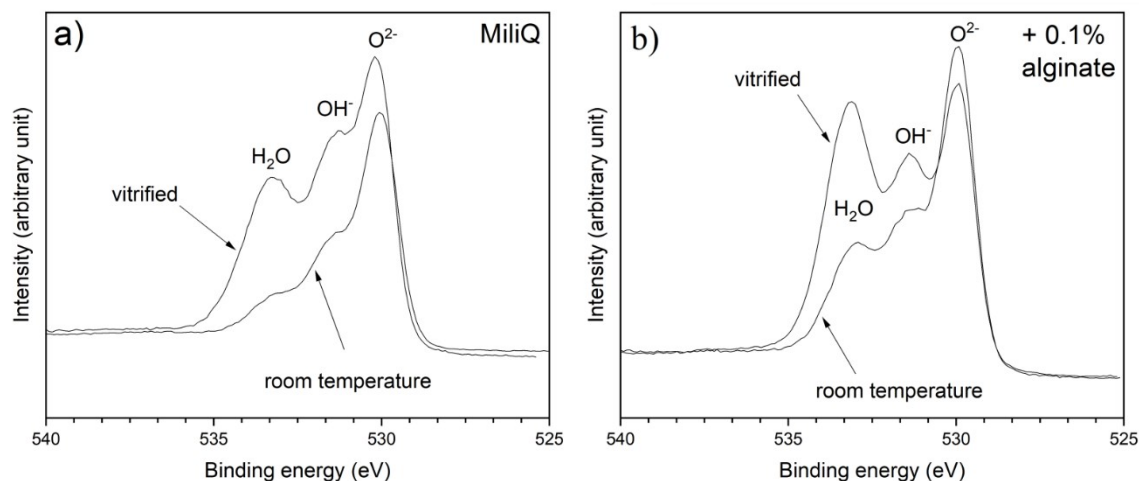
Figure S9. High-resolution XPS spectra of O 1s region for a) pure hematite and b) alginate-hematite complex. O^{2-} structural oxygen from hematite, OH^- - hydroxyl groups in the hematite-solution interface region and H_2O- interfacial water

11. Persistence length

The persistence length of polymers depends on the molecular weight,[13] polymer composition,[14–16] linearity or the degree of polymer branching,[17,18] the polymer concentration in the studied solution,[16] the background electrolyte[19] and its ionic strength.[14,19–21] Alginate is not an exception.[14,15,22] Reported values of persistence length for alginate range from 0.5 nm to 30 nm, with the values higher than 10 nm being exclusively derived from measurements where the intrinsic viscosity is measured at low polymer concentration (and often higher molecular weight, e.g.[15]) which has been shown to significantly increase the persistence length.

We used alginate with a molecular weight between 75-200 kDa, where at least 50% of monomeric units were mannuronate. The Lp values obtained from our worm-like chain fits yield the values shown in Fig. S10A for alginate and S10B for EPS. The histogram of Lp prior to filtering the data are presented in Fig. S10C. The values above 4×10^{-9} m show a poor fit and using an extended worm-like chain fit or freely jointed chain models did not improve the fit statistics for those curves. Hence, considering the low molecular weight of the alginate used in this study and the high density of the polymers of the tip, the curves with Lp values between 1-4 nm are considered to approximate single polymer events.
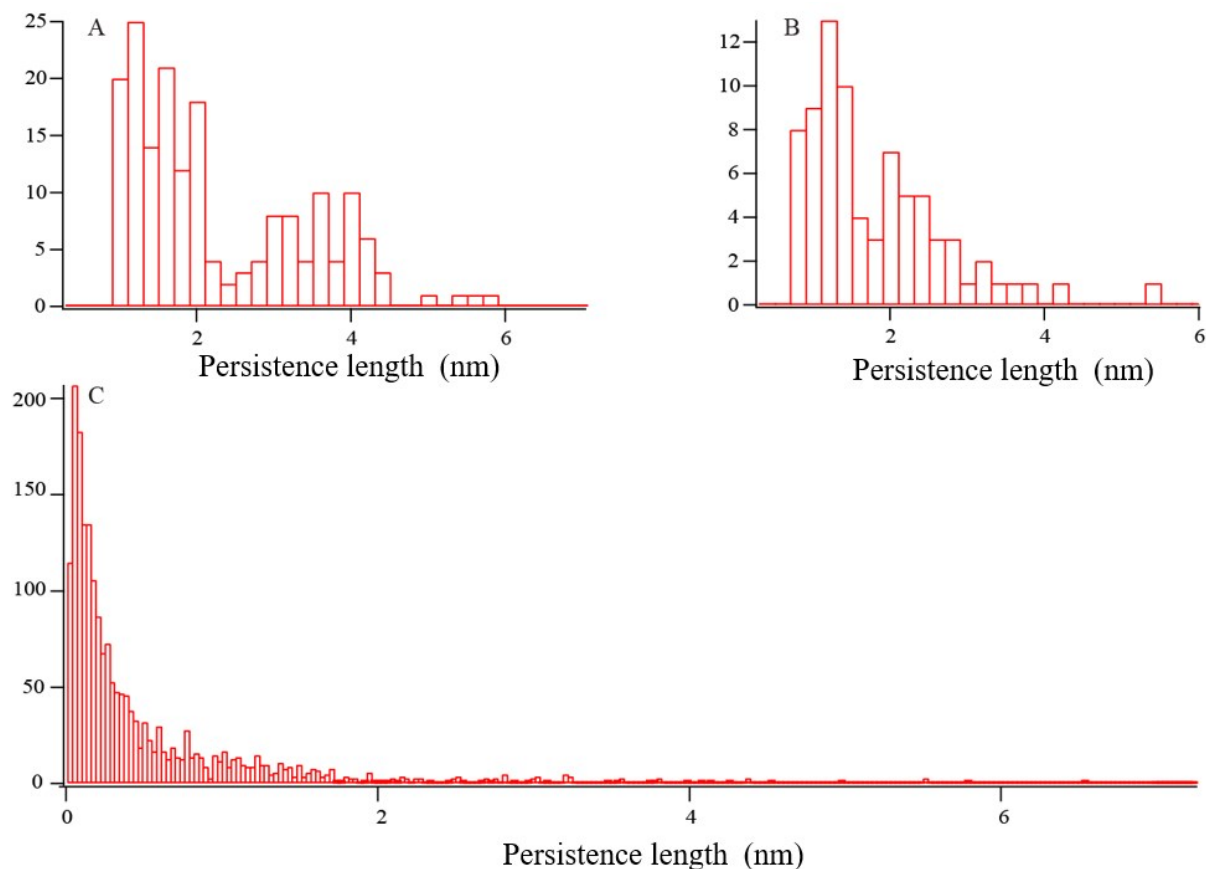
Figure S10. Distribution of used values for persistence length for A) alginate and B) EPS. C) Distribution of persistence length values pre-filtering (i.e. all obtained force curves that were fitted to the worm-like chain model). The bimodality for A and B is expected because of the complex system we are measuring. First of all, the position of the COO^- group from the biopolymers that is bound to the short linker molecules will vary across the polymer brush, secondly, we are likely to have several types of interactions (H-bonding and electrostatic) between the polymers and the mineral surface and third, because of the polymer brush we will have polymer-polymer interactions going on as well (H-bonding, Van der Waals, steric and electrostatic forces) leaving a weaker charge to interact with the iron oxide..
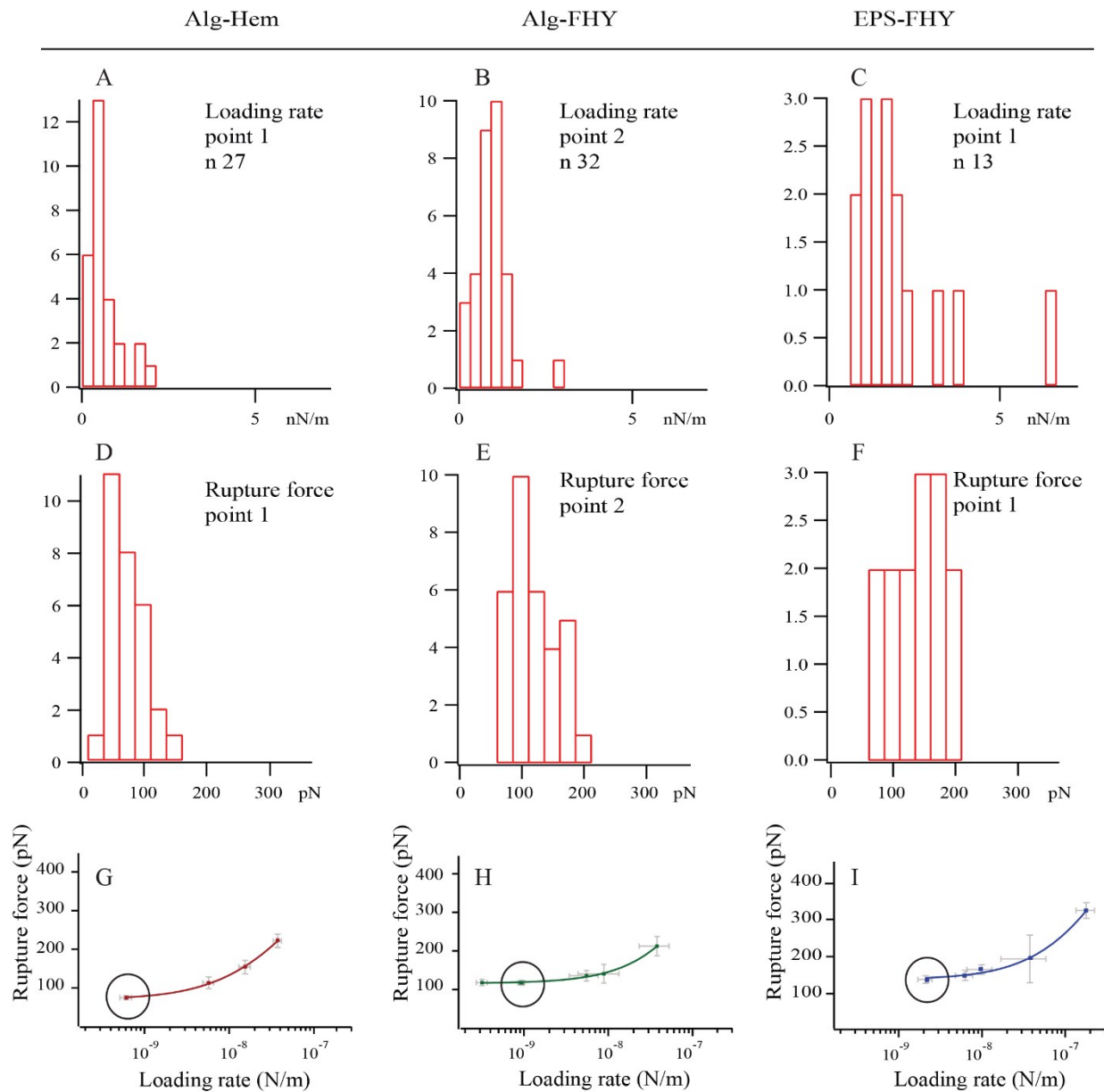
Figure S11. Histograms of the distribution of A-C) loading rate and D-F) rupture force for points in the equilibrium regime for each experimental data set (row). G-I) The chosen point in the DFS plot is important for determining the f_{eq} value.

12. XPS of alginate coated MSCT tips

We used XPS to ensure that the MSCT tips were successfully functionalized. The spectrum shows elements attributed to the underlying tip (Si), trimethoxysilylpropyl-diethylenetriamine linker (Si, N, O, C), EDAC linker (C, N) and alginate (C, O) (Figure S12a). Comparison between the high-resolution spectra of C 1s region (Figure S12b) of the alginate powder (red line) and the alginate coated tip (black line) shows **a)** that the C-H peak (285 eV) is more intense in alginate coated MSCT spectra than in pure alginate which is expected considering that both linkers contain C-H bonds and **b)** that there are carboxyl (~288 eV) and hydroxyl (~286.5 eV) groups present on the tip's surface. b) suggests that the alginate is part of the SAM because carboxyl and hydroxyl groups are present in alginate but not in compounds that link tip surface to alginate. The absence of the Na KLL line from the O 1s region of the alginate coated MSCT tip indicates that the alginate was solubilized prior to its linking in the SAM (Figure S12c). Because of strong contribution of O from the trimethoxysilylpropyl-diethylenetriamine linker, we were not able to fully decompose the O 1s peak to look into the behavior of alginate's carboxyl and hydroxyl groups within the SAM. However, the carboxyl and hydroxyl environments in the alginate powder and alginate within the SAM must be similar or else we would observe a significant change in the C 1s region. Finally, Figure S12d and S12e confirm that both trimethoxysilylpropyl-diethylenetriamine and EDAC linkers are part of the SAM.
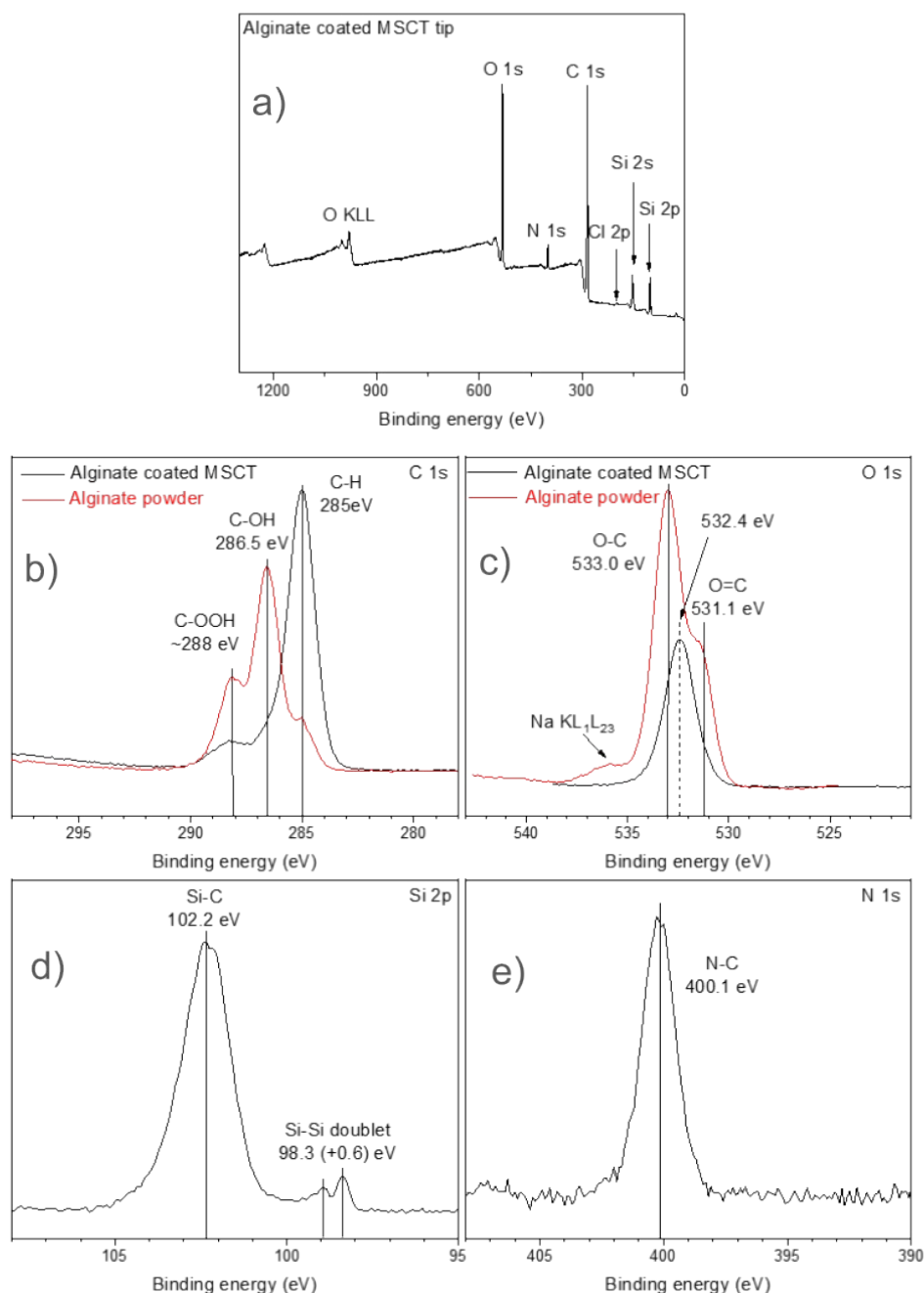
Figure S12. XPS spectra of alginate coated MSCT tip (black line) and alginate powder (red line). A) wide spectrum of alginate coated MSCT tip. Comparison of high-resolution spectra of alginate coated MSCT tips and alginate powder for b) C 1s region and c) O 1s region. High-resolution spectra of alginate coated MSCT tip for d) Si 2p showing strong contribution from Si-O-C environment and weak from underlying elemental Si substrate, and e) N 1s region showing only N-C binding environment. The peak assignment was taken from the literature.[23–25]

13. Approximating free energy per unit length with equilibrium force

As briefly discussed in the main manuscript, in the near equilibrium pulling, γ is related to the external load, f, by[26,27]

$$\gamma = \frac{k_B T}{b} \ln \left(\frac{4\pi \sinh (F)}{F} \right),$$

where b is the Kuhn length of the polymer and

$$F = \frac{fb}{k_B T},$$

is a dimensionless force. For large values of F[26]

$$\ln \left(\frac{4\pi \sinh (F)}{F} \right) \approx \ln (4\pi) + F - \ln (F) \approx F,$$

and, therefore, we arrive at the approximation,

$$\gamma \approx f$$

14. References

1. Schwertmann, U. & Cornell, R. M. Iron Oxides in the Laboratory Preparation and Characterization. (1991).

2. Michel, F. M. *et al.* Ordered ferrimagnetic form of ferrihydrite reveals links among structure, composition, and magnetism. *Proc. Natl. Acad. Sci.* **107**, 2787–2792 (2010).

3. Hiemstra, T. & Van Riemsdijk, W. H. A surface structural model for ferrihydrite I: Sites related to primary charge, molar mass, and mass density. *Geochim. Cosmochim. Acta* **73**, 4423–4436 (2009).

4. Waychunas, G. *et al.* Surface complexation studied via combined grazing-incidence EXAFS and surface diffraction: arsenate on hematite (0001) and (10–12). *Anal. Bioanal. Chem.* **386**, 2255–2255 (2006).

5. Friddle, R. W., Noy, A. & De Yoreo, J. J. Interpreting the widespread nonlinear force spectra of intermolecular bonds. *Proc. Natl. Acad. Sci.* **109**, 13573–13578 (2012).

6. Majzlan, J., Navrotsky, A. & Schwertmann, U. Thermodynamics of iron oxides: Part III. Enthalpies of formation and stability of ferrihydrite (∼Fe(OH)3), schwertmannite (∼FeO(OH)3/4(SO4)1/8), and ε-Fe2O3 1. *Geochim. Cosmochim. Acta* **68**, 1049–1059 (2004).

7. Trolard, F. & Tardy, Y. Stabilities of Gibbsite, Boehmite, Aluminous Goethites and Aluminous Hematites in Bauxites, Ferricretes and Laterites as a Function of Water Activity, Temperature and Particle Size. *Geochim Cosmochim Acta U. S.* **51:4**, (1987).

8. Söhnel, O. Estimation of electrolyte-crystal-aqueous-solution interfacial tension. *J. Cryst. Growth* **63**, 174–176 (1983).

9. Williams, M. A. K., Marshall, A., Haverkamp, R. G. & Draget, K. I. Stretching single polysaccharide molecules using AFM: A potential method for the investigation of the intermolecular uronate distribution of alginate? *Food Hydrocoll.* **22**, 18–23 (2008).

10. Michel, F. M. *et al.* The structure of ferrihydrite, a nanocrystalline material. *Science* **316**, 1726–1729 (2007).

11. Michel, F. M. *et al.* Similarities in 2-and 6-line ferrihydrite based on pair distribution function analysis of X-ray total scattering. *Chem. Mater.* **19**, 1489–1496 (2007).

12. Shchukarev, A. & Boily, J.-F. XPS study of the hematite–aqueous solution interface. *Surface and Interface Analysis* https://onlinelibrary.wiley.com/doi/abs/10.1002/sia.2657 (2008) doi:10.1002/sia.2657.

13. Rinaudo, M. & Noik, C. Adsorption of polysaccharides on a calcite using spin labeled polymers. *Polym. Bull.* **9**, 543–547 (1983).

14. Hecht, H. & Srebnik, S. Structural Characterization of Sodium Alginate and Calcium Alginate. *Biomacromolecules* **17**, 2160–2167 (2016).

15. Vold, I. M. N., Kristiansen, K. A. & Christensen, B. E. A Study of the Chain Stiffness and Extension of Alginates, in Vitro Epimerized Alginates, and Periodate-Oxidized Alginates Using Size-Exclusion Chromatography Combined with Light Scattering and Viscosity Detectors. *Biomacromolecules* **7**, 2136–2146 (2006).

16. Josef, E. & Bianco-Peled, H. Conformation of a natural polyelectrolyte in semidilute solutions with no added salt. *Soft Matter* **8**, 9156–9165 (2012).

17. Lecommandoux, S. *et al.* Effect of Dense Grafting on the Backbone Conformation of Bottlebrush Polymers: Determination of the Persistence Length in Solution. *Macromolecules* **35**, 8878–8881 (2002).

18. Ramachandran, R. *et al.* Persistence Length of Short-Chain Branched Polyethylene. *Macromolecules* **41**, 9802–9806 (2008).

19. Brunet, A. *et al.* Dependence of DNA Persistence Length on Ionic Strength of Solutions with Monovalent and Divalent Salts: A Joint Theory–Experiment Study. *Macromolecules* **48**, 3641–3652 (2015).

20. Rinaudo, M., Milas, M. & Dung, P. L. Characterization of chitosan. Influence of ionic strength and degree of acetylation on chain expansion. *Int. J. Biol. Macromol.* **15**, 281–285 (1993).

21. Tricot, M. Comparison of experimental and theoretical persistence length of some polyelectrolytes at various ionic strengths. *Macromolecules* **17**, 1698–1704 (1984).

22. Baños, F. G. D. *et al.* Influence of ionic strength on the flexibility of alginate studied by size exclusion chromatography. *Carbohydr. Polym.* **102**, 223–230 (2014).

23. Moulder, J. F., Stickle, W. F., Sobol, P. E. & Bomben, K. D. *Handbook of X-Ray Photoelectron Spectroscopy. A Reference Book of Standard Spectra for Identification and Interpretation of XPS Data*. (Perkin-Elmer Corporation, 1992).

24. Lim, S.-F., Zheng, Y.-M., Zou, S.-W. & Chen, J. P. Characterization of Copper Adsorption onto an Alginate Encapsulated Magnetic Sorbent by a Combined FT-IR, XPS, and Mathematical Modeling Study. *Environ. Sci. Technol.* **42**, 2551–2556 (2008).

25. Dietrich, P. M. *et al.* Quantification of Silane Molecules on Oxidized Silicon: Are there Options for a Traceable and Absolute Determination? *Anal. Chem.* **87**, 10117–10124 (2015).

26. Manohar, S. *et al.* Peeling Single-Stranded DNA from Graphite Surface to Determine Oligonucleotide Binding Energy by Force Spectroscopy. *Nano Lett.* **8**, 4365–4372 (2008).

27. Manohar, S. & Jagota, A. Sequence-dependent force response during peeling of single-stranded DNA from graphite. *Phys. Rev. E Stat. Nonlin. Soft Matter Phys.* **81**, 021805 (2010).